Metal decontamination by high repetition rate nanosecond fiber laser: Application to oxidized and Eu-contaminated stainless steel

L. Carvalho, W. Pacquentin, M. Tabarant, A. Semerok, H. Maskrot

Metal decontamination by high repetition rate nanosecond fiber laser: application to oxidized and Eu-contaminated stainless steel

L. Carvalho, W. Pacquentin*, M. Tabarant, A. Semerok, H. Maskrot

Des Service d'Etudes Analytiques et de Réactivité des Surfaces (SEARS), CEA, Université Paris-Saclay, F-91191, Gif sur Yvette, France

Abstract

The decommissioning of metallic equipment (pipes, lane surfaces, etc.) contaminated in nuclear installations can consign large amounts of waste to storage and risk workers to radioactive exposure. Here, we study metallic-surface decontamination by laser ablation, which involves ejection and subsequent trapping of surface contamination by subjecting the surface to high-energy laser pulses. We perform laser ablation on oxidized AISI 304L stainless steel samples impregnated with non-radioactive Eu using a high repetition rate nanosecond fiber laser. The oxide layers are with a mean weight percentage of 0.1 to 2% of Eu in the volume of the oxide layer. Glow discharge mass spectrometry (GDMS) is performed to assess the cleaning-treatment efficiency and study the distribution of residual contamination with a Eu-detection limit of 100 *ng/g*. Our results indicate satisfactory decontamination of up to 97%. We also study the limiting factors and identify the mechanism of penetration of contaminants as induced by thermal effects. Moreover, to understand the ablation mechanism and from the perspective of industrial applications, we analyze the ablated matter to obtain the particle chemical composition and size distributions.

Keywords: laser cleaning, laser ablation, Eu in-diffusion, oxide layer, decontamination, residual contamination

**Corresponding author*
Email address: wilfried.pacquentin@cea.fr

1. Introduction

The decontamination of components and equipment (such as steam generators and pipes) in nuclear facilities forms a necessary step in their decommissioning. This decontamination involves separating radioactive contaminants from the cleaned structures. The objective is to mainly reduce worker exposure to stray radiation and avoid the spreading of radioactive contaminants. In this regard, a priority for nuclear safety authorities, operators, and governments is the development of safer decontamination techniques [1]. In this context, current mechanical surface removal and chemical treatments suffer from many disadvantages; these techniques are labor-intensive, can expose workers to radiation, and can generate a large volume of secondary wastes such as hazardous and radioactive chemical solutions that need long-term storage [2]. In the case of metallic structures, the contaminants can be either attached to the surface by weak Van der Waals forces [3] or located in the oxide layer[4][5] In both cases, only a small volume of contaminated material needs to be removed and treated.

In this framework, lasers are already being used in a wide range of surface treatment processes for coating depositions [6] or microelectronics cleaning [7], and further, lasers can successfully decontaminate concrete [8], painted surfaces [9], and metallic components [3][5][10][11][12][13][14][15][16][17][18]. Laser cleaning offers several advantages: it reduces the amount of radioactive waste, the laser can be remotely operated (thereby preventing worker exposure), and further, as a dry treatment method, laser cleaning generates no secondary waste. The principle underlying laser cleaning is the ablation of the contaminated layer by a nanosecond pulsed laser directed to the surface and the collection and storage of the ejected contamination.

The regime of interaction between the laser source and a metallic surface with an oxide layer depends strongly on the characteristics of the laser beam [19][20] (wavelength, pulse duration, energy density, etc.), the surface state (factors of roughness, absorption, etc.), and the ambient environment (liquid layer, gas atmosphere). In the case of a nanosecond-pulse regime, the mass removal is mainly induced by thermal effects [19][21][22][23][24]. Here, the laser energy absorbed by electrons (free for metal or bounded for oxide) is converted into heat in the metal/oxide lattice. The electrons temperature is considered equal to the lattice temperature. The resulting thermal conduction leads to fast and localized heating, melting, and vaporization of

the target surface. Once ablated, the particles can be collected to avoid their deposition on the surface and undesired absorption of the laser beam.
The goals of our work are to highlight the performance of the laser cleaning technique as applied to oxidized and contaminated stainless steel with the use of a high-repetition-rate nanosecond pulsed fiber laser and identify the mechanism of ablation during laser treatment. In this study, we particularly focused on the sample preparation and characterization along with multiparametric optimization of the laser cleaning parameters. We also discuss the obtained results from the perspective of understanding the cleaning performance and ablation mechanisms.

2. Material and methods

We carried out a cleaning study with a nanosecond pulsed ytterbium fiber laser on non-radioactive Eu-contaminated and oxidized stainless steel AISI 304L specimens. The cleaning efficiency was obtained by analyzing the evolution of the Eu concentration via glow discharge mass spectrometry (GD-MS). The chemical composition and dimensions of the ejected particles were also analyzed to assess the ablation mechanism.

2.1. Laser cleaning prototype

As shown in Figure 1, the laser setup is composed of an ytterbium fiber laser[1], an X–Y galvanometric scanning system[2], and a focusing lens[3] (λ = 1064 *nm*, f = 330 *mm*) resulting in a laser beam waist radius of ω = 62 ± 2 μm (at $1/e^2$ intensity level). The laser source is a Gaussian beam (M^2=1.4) with a wavelength of λ = 1064 *nm*, pulse duration of τ = 120 *ns* at full-width at half maximum (FWHM), and 15 *W* of maximal average power (0.75 *mJ* per pulse, repetition rate ν = 20 *kHz*). From the perspective of the usage of nanosecond pulsed lasers in industrial processes, we chose the Yb fiber laser because of its low maintenance cost, reliability, and compactness [25][26][27][18]. Such laser system was successfully applied for cleaning the tokamak vessel walls [25][26] and mirrors [27][18]. In the study, the laser power P was varied between 6 and 15 *W* to obtain a maximal fluence per pulse F in the range of 5.0 to 12.4 J/cm^2 along the beam axis. In order to avoid re-deposition of the contamination and to collect the ejected particles, the samples were

[1] IPG YLP-1/120/20
[2] SCAN LAB SCANcube 10
[3] Linos F-Theta Ronar

treated in an ablation cell with a volume of 151 cm^3 with an ambient air flow of 3.0 L/min.

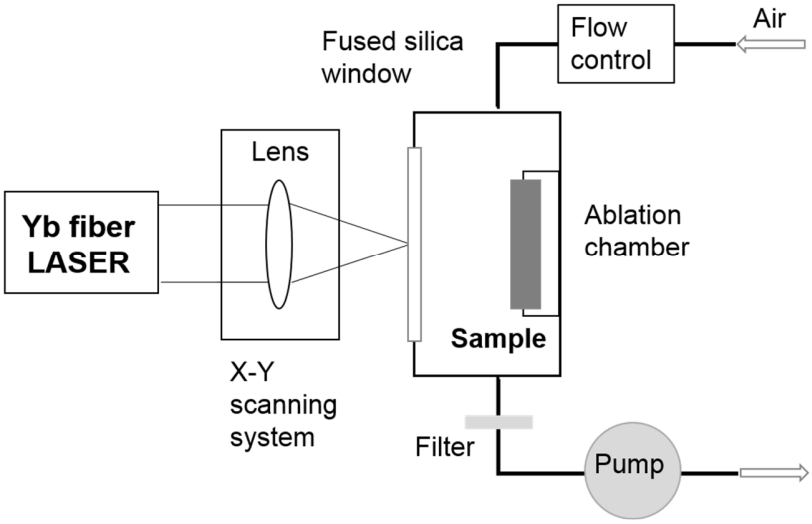

Figure 1. Schematic of ablation cell used in study

The sample surface is placed at the focal position of the focusing lens. Laser treatments are performed for a large range of total energy delivered by surface unit, E in J/cm^2, which is controlled in practice by the mean power of laser beam P and the speed of the sample scanning u. The maximal laser fluence per pulse along the beam axis, $F\ (J/cm^2)$, is defined as the laser energy per surface unit:

$$F = \frac{2\,P}{\nu\,\pi\,\omega^2} \tag{1}$$

Surface scanning was performed with the application of a snake-like pattern resulting from scanning along parallel horizontal lines, which was defined by the parameters of scanning speed u (mm/s) and vertical step Δy (mm) between two lines. These parameters were chosen to provide the desired spatial overlapping R between two successive laser spots:

$$u = 2\omega\nu\left(1 - \frac{R}{100\%}\right) \tag{2}$$

$$\Delta y = 2\omega\left(1 - \frac{R}{100\%}\right) \tag{3}$$

The treatment resulted in the delivery of a total delivered energy per unit surface area of E (J/cm^2), calculated as follows:

$$E = \frac{P\ \Delta t}{S} \tag{4}$$

where Δt (s) is the total treatment duration and S (cm^2) refers to the treated sample surface area.

2.2. Analytical techniques

The composition and structure of the oxidized samples were characterized and analyzed before and after laser treatment by use of complementary techniques. The surface was observed by use of a scanning electron microscope [4] (SEM) operated in two detection modes: backscattering electron (BSE) and secondary electron (SE) modes. The oxide composition was determined by means of X-ray diffraction [5] (XRD). The element distribution along the depth direction was monitored via glow discharge mass spectrometry [6] (GD-MS). After treatment, the collected particles were chemically characterized by means of inductively coupled plasma/optical emission spectrometry[7] (ICP-OES).

2.3. Sample preparation

In order to study the laser cleaning of metallic equipment used in nuclear facilities, we chose samples of AISI 304L stainless steel (304L SS) with a non-radioactive level of Eu contamination as the simulation of a fission product of uranium (U). The controlled incorporation of Eu into the steel specimens allowed us to obtain the desired contamination distribution along the depth direction for a better understanding of the cleaning process and also overcoming the constraints of working in a radioactive environment. Oxide layers were prepared through laser oxidation on 304L SS samples that were cold-rolled and cut by water jets into specimen sizes of 30 mm × 30 mm × 3 mm. The chemical composition of the 304L SS samples as obtained by ICP-OES is listed in Table 1. Further, GD-MS analysis of the metallic bulk showed that no Eu was initially present within a detection limit of 100 ng/g.

[4] SEM-FEG JEOL JSM-7000F
[5] Bruker D8 Advance
[6] Thermo Scientific Element GD Plus
[7] Perkin Elmer Optimal 8300 DV

Element	Fe	Cr	Ni	Mn	Si	Cu	Co	Mo
Weight concentration (%)	68.87	18.57	9.23	1.41	0.86	0.59	0.22	0.22

Table 1. Chemical composition of AISI 304L stainless steel samples as obtained by inductively coupled plasma/optical emission spectrometry (ICP-OES)

After cleaning in an ultrasound bath with ethanol, the specimens were "contaminated" by nebulization of a solution of $Eu(NO_3)_3$ in water at a Eu concentration of 4000 *mg/L*.

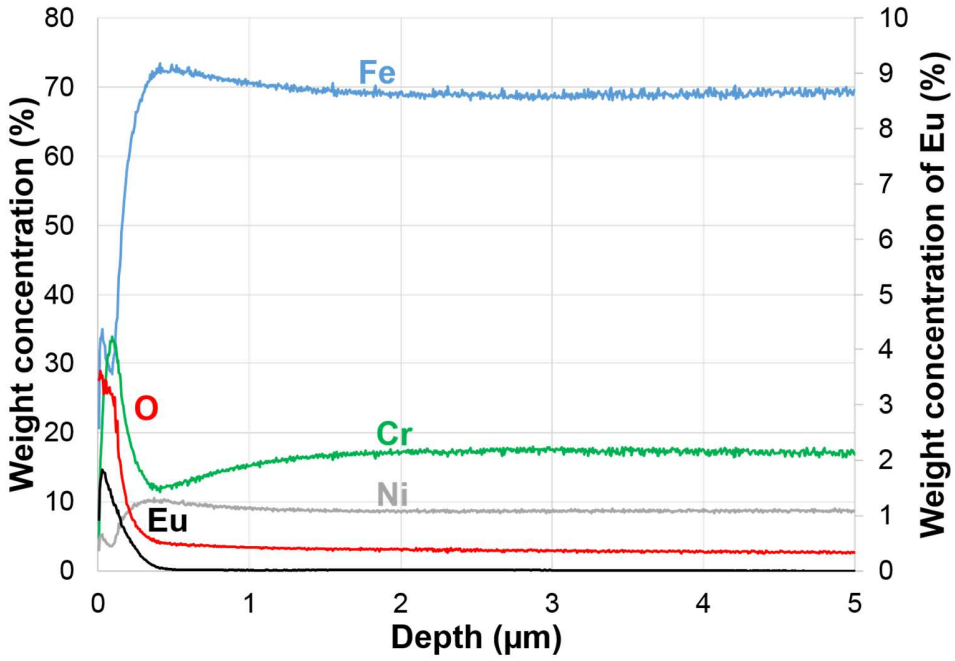

Figure 2. Glow discharge mass spectrometry (GD-MS) profile of oxidized sample before cleaning

Oxidation was performed by laser irradiation at atmospheric pressure with the previously described laser setup (section 2.1) with a focusing lens with f = 420 *mm*, laser beam waist radius ω = 84 ± 2 μm, laser fluence of F = 6.1 J/cm^2, and scanning speed of 348 *mm/s*, corresponding to a spatial overlap of 90%. The use of a larger laser beam afforded a lower laser energy density, and the setup was used to heat the surface and induce oxidation. The details of the oxidation procedure are provided in our study [28][29].

2.4. Characterization of oxide layers

The depth-wise element distribution of the studied oxide layer is presented in Figure 2. The oxide thickness was determined to be 0.13 ± 0.03 μm with contamination of Eu over the entire volume of the oxide with an average weight concentration of 0.95 ± 0.45%. The oxide thickness is determined using the GDMS in-depth profile. The glow discharge mass spectroscopy gives the elementary composition of the sample as a function of the erosion time of the surface. Using measurements standards as metal oxides and metallic bulks, the erosion time can be evaluated as a function of the analyzed depth [30] , The interface between the oxide layer and the metallic bulk was evaluated by analysis of the GD-MS profile and defined as the depth at which the density of the material was 0.9 times the density of 304L SS.

XRD analysis ($\lambda_{CuK\alpha}$ = 1.54 Å, grazing incidence, θ = 1°) of the Eu-contaminated and oxidized sample indicated the formation of mainly Fe_3O_4 (JCPDS 00-019-0629) and/or $FeCr_2O_4$ (JCPDS 00-024-0512) in the oxide layer but no specific oxide of Eu was observed. Here, we remark that the same oxides have been previously observed when analyzing a sample oxidized under the same conditions without any contamination [31]. The GD-MS profile of the sample (Figure 2) highlights the presence of both Fe and Cr in the oxide layer. Moreover, Fe_3O_4 and $FeCr_2O_4$ have similar crystallographic structures, which makes it difficult to differentiate between the two responses. The formation of an oxide composed of Fe, Cr, and Eu was assumed but the concentration of Eu was too low to be detected with this technique.

Laser energy absorption by the sample surface is a main factor of cleaning efficiency. The optical absorbance were thereby determined by use of an integrating sphere for blank and oxidized 304L SS samples with a laser source with wavelength λ = 1064 nm. A photodiode connected to an oscilloscope is placed inside a highly diffusive optical cavity. The optical cavity has two apertures. One of them is used as the laser source beam entry. Firstly, the other aperture is closed and the signal is measured as the reference of total reflectivity. Then the sample is placed in front of the aperture and the signal is measured. The reflectivity is defined as the ration between the sample signal and the reference. The absorbances were determined as 29 ± 2% for the blank metal and 74 ± 1% for the oxidized and Eu-contaminated samples.

The decontamination fluence threshold was defined as the minimal fluence that needs to be delivered at the sample surface to initiate ablation of the whole oxide layer thickness by one laser shot. This parameter was experimentally assessed by observation of the dimensions of the ablation crater after application of one laser pulse while varying the laser energy. The measurement of the inner diameter of the ablation craters, measured at the surface level, was performed by means of an optical microscope [8] at a magnification of ×50 (Figure 3).

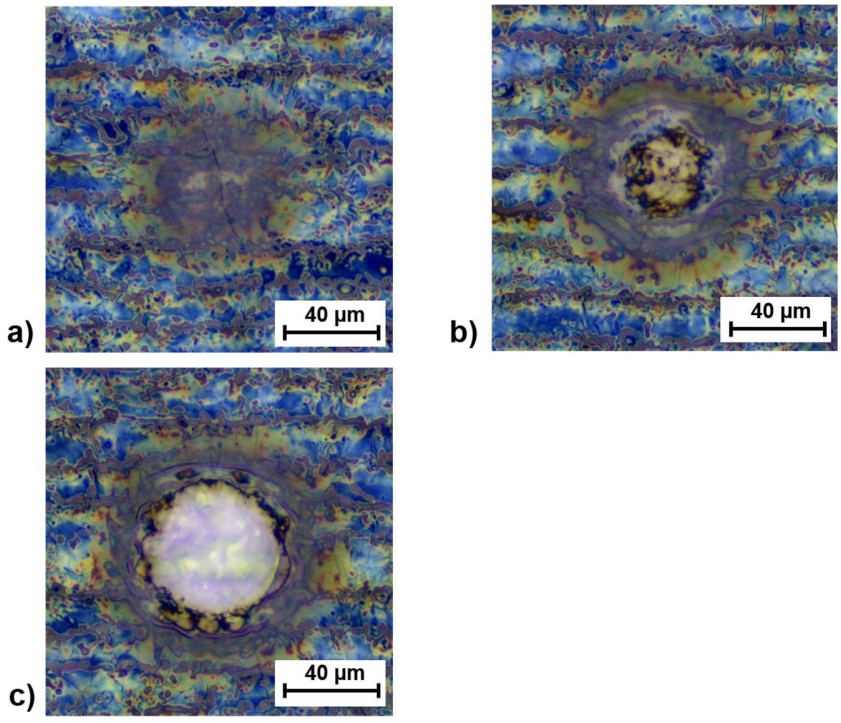

Figure 3. Images (M = ×50) of ablation craters after application of one laser pulse for fluences of: (a) 3.3 J/cm²; (b) 5.0 J/cm²; (c) 6.6 J/cm²

The oxide layer decontamination threshold F_{th} was determined by fitting the evolution of the square of the inner diameter D^2 as a function of the laser fluence per pulse F as follows [32][33](Figure 4):

$$D^2 = 2\omega^2 \ln(F/F_{th}) \quad (5)$$

[8] Zeiss

The decontamination fluence threshold corresponds to laser fluence giving D=0 and it was determined to be 5.0±0.1 J/cm^2. The range of laser fluence studied was assessed based on the decontamination threshold of the oxidized sample.

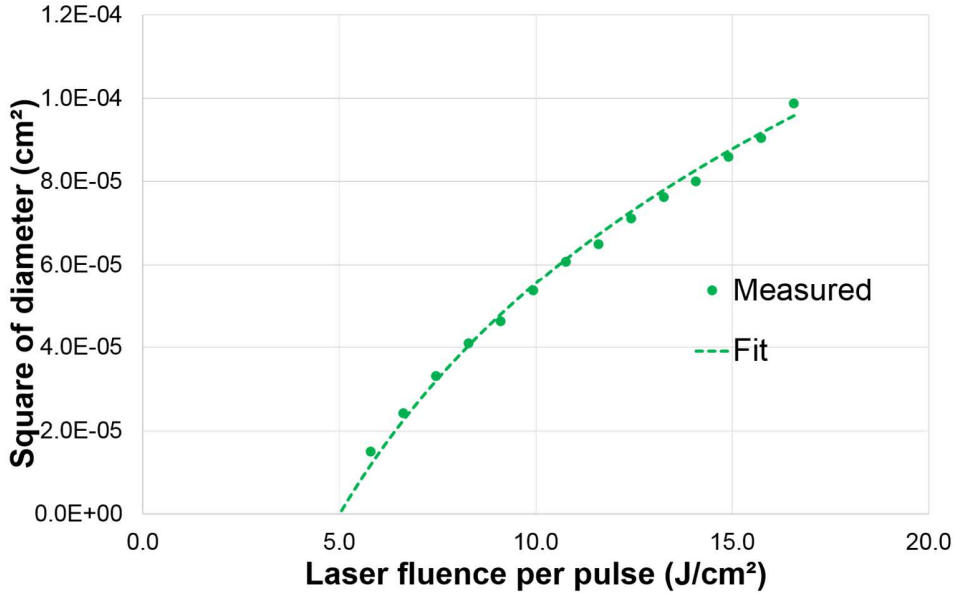

Figure 4. Evolution of square of diameter of ablation hole as function of laser fluence

2.5. Size distribution of ablated matter

The size distribution of the removed matter was obtained by use of a cascade impactor [9] (electrical low-pressure impactor, ELPI). During the cleaning treatment, ablated matter was transported to the top of the ELPI by means of a vacuum pump and electrically charged in an ambient atmosphere. After charging, the particles were collected at the different impactor stages according to their aerodynamic diameter d_a over the range of 6 nm to 10 μm. The experiments were performed with the standard parameters of the equipment: a corona charger tension of 5kV, a sensor pressure of 40 mbar and an air flow of 3L/min. The maximal concentration of particles per measuring time (1 s) is between $1.7x10^7$ particle/cm^3 for the smallest stage

[9] ELPI Classic, DEKATI

($D_{50\%}$=0.04 µm) and 2.4x10^4 particle/cm^3 for the biggest stage ($D_{50\%}$=8.2 µm). This measurement resulted in the obtainment of the size distribution, and it was accompanied by the collection of aerosols on polycarbonate filters (25 mm diameter, 0.2 μm pore size, Whatmann) for offline SEM characterization in the backscattering electron detection mode (SEM-BSE).

3. Results and discussion

3.1. Cleaning efficiency

Cleaning tests were performed with the laser beam fluence being varied from F = 5.0 up to 12.4 J/cm^2 and a scanning speed range of u = 244 to 976 mm/s, corresponding, respectively, to a spatial overlap between R = 90% and 60%. Treated zones of 30 mm × 30 mm were analyzed via GD-MS in order to determine the cleaning efficiency. Cleaning efficiency CE is determined as the ratio of the contaminant mass after and before cleaning treatment (Eq. (6)). In the study, the mass of contaminant was assessed by the integration of the Eu signal obtained by GD-MS for the first 5 μm of the sample, and the cleaning efficiency was calculated as follows:

$$CE = \frac{M_{initial}^{Eu} - M_{final}^{Eu}}{M_{initial}^{Eu}} \times 100 \quad (6)$$

Figure 5 displays the evolution of the decontamination or cleaning efficiency as a function of the accumulated energy per unit surface area on the sample surface as calculated using Eq. (4). The percentage of removed contamination is represented for every pair of the parameters of interest: laser beam fluence and scanning speed. To aid better reader comprehension, the laser parameters of the treatments of interest are summarized in Table 2. We note from the table that after one scan of the surface, up to 97% of the Eu contamination was ablated with Treatment 4.

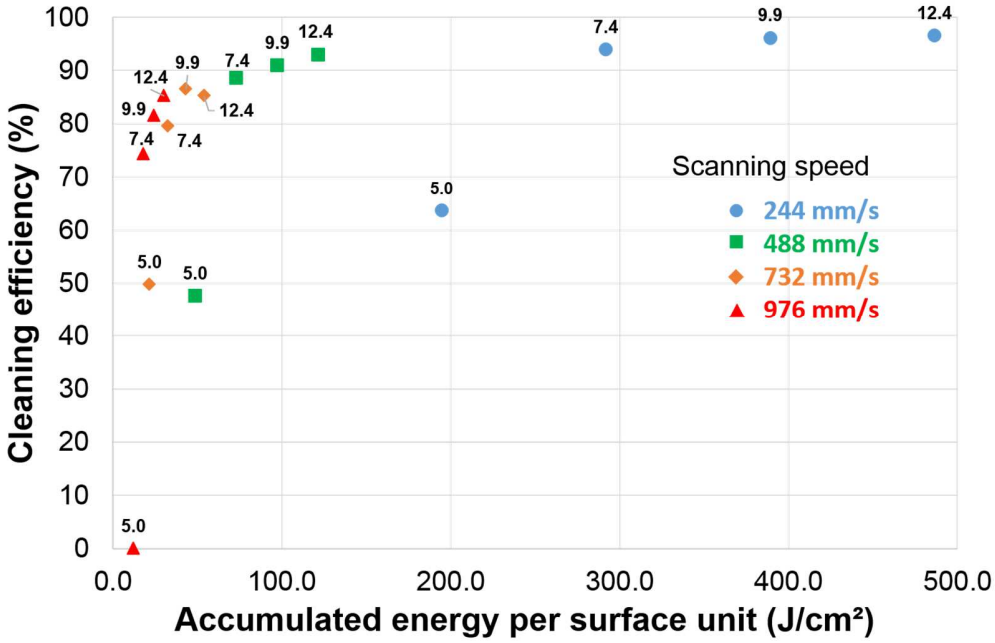

Figure 5. Decontamination efficiency CE as function of accumulated laser energy per unit surface area, E (J/cm^2), on surface sample. The number above each symbol represents the laser fluence per pulse, F(J/cm^2).

Treatment No.	Laser Fluence per pulse F (J/cm^2)	Scanning speed u (mm/s)	Spatial overlap R (%)	Total laser energy E (J/cm^2)	Cleaning efficiency CE (%)
1	5.0	976	60	12.2	0
2	5.0	488	80	48.6	48±2
3	12.4	488	80	121.6	93±1
4	12.4	244	90	486.4	97±1

Table 2. Laser parameters of cleaning treatments of interest

The results presented in Figure 5 highlight the efficacies of the different cleaning regimes according to the scanning speed. For a laser fluence of 5.0 J/cm^2, the decontamination is not efficient since the fluence is near the decontamination threshold. The GD-MS profile of the oxidized sample after

laser treatment 1 (Figure 6) shows that at the decontamination fluence threshold, the oxide layer is not completely removed. The decontamination at the decontamination threshold laser fluence resulting from treatment 2 (Figure 7) is assumed to be due to the high spatial overlap between laser spots, thus leading to heat accumulation on the treated surface and decrement in the ablation threshold [18][34], making the decontamination possible. The remaining oxide layer in the case of treatment 2 (Figure 7) can be explained by the fact that the ablated thickness is <0.13 μm and by the re-oxidation of the surface by laser heating, particularly at high spatial overlap values. The cleaning efficiency appears to increase with the accumulated energy per surface unit for a range of total accumulated energy per surface E up to 150 J/cm^2. Indeed, when the laser fluence is increased to 12.4 J/cm^2 (treatment 3), the contamination ejection is almost complete without the formation of a secondary oxide layer (Figure 8) that could trap residual contamination. However, the augmentation of the accumulated energy by the use of a lower scanning speed of 244 mm/s (Figure 9) afforded a different decontamination regime characterized by limitation of the efficiency. That is, treatment 4 affords an efficiency gain of 3.7% relative to that of treatment 3 for twice the accumulated energy and duration of treatment of the sample. In this case, more criteria such as the duration of the laser treatment and the energy resources need to be defined to determine the optimal laser parameters. These criteria will significantly impact the final cost of the cleaning operation.

The saturation of decontamination (Figure 5) appears to be the consequence of modification of the laser source absorption by the treated surface. Surface absorbance was found of 16±1% after treatment 3 and of 73±7% after treatment 4. This effect can be induced either by sample surface modification in case of a high spatial overlap or the screening effect caused by the amount of ablated matter. Indeed, SEM observations of the sample surface after treatment 3 (Figure 10) and treatment 4 (Figure 11) indicate that the change in scanning speed led to a different surface texturing and possibly different absorption of the laser energy. As for the ablation mechanism underlying the decontamination treatment, from the SEM-SE image in Figure 10, we note that laser decontamination leads to structural modification of the surface by superficial fusion and vaporization. The observed surface wave structures are the proof of the formation and ejection of a liquid layer of 1-2 μm thickness during laser irradiation.

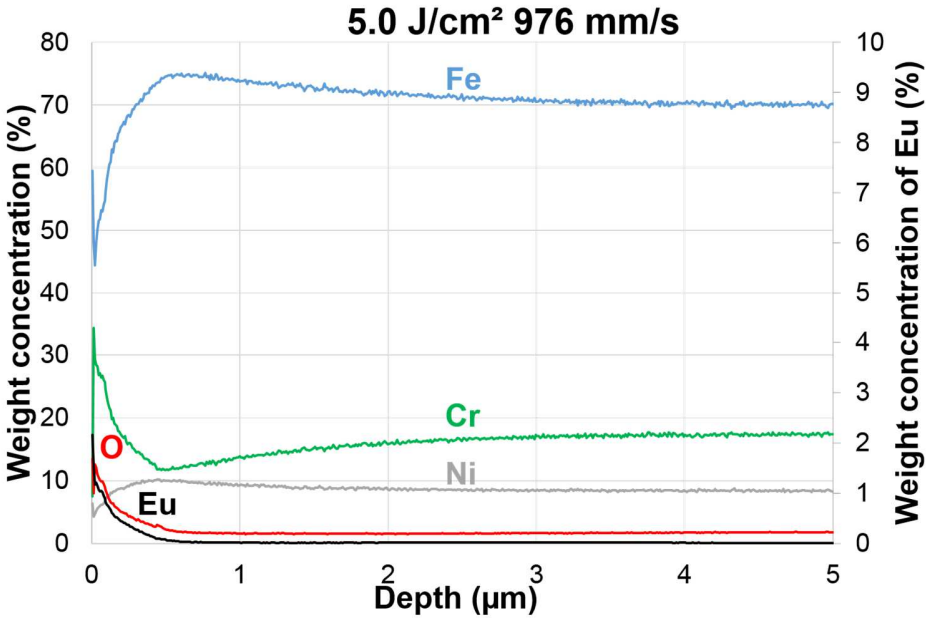

Figure 6. Glow discharge mass spectrometry (GD-MS) profile of oxidized sample after laser treatment 1

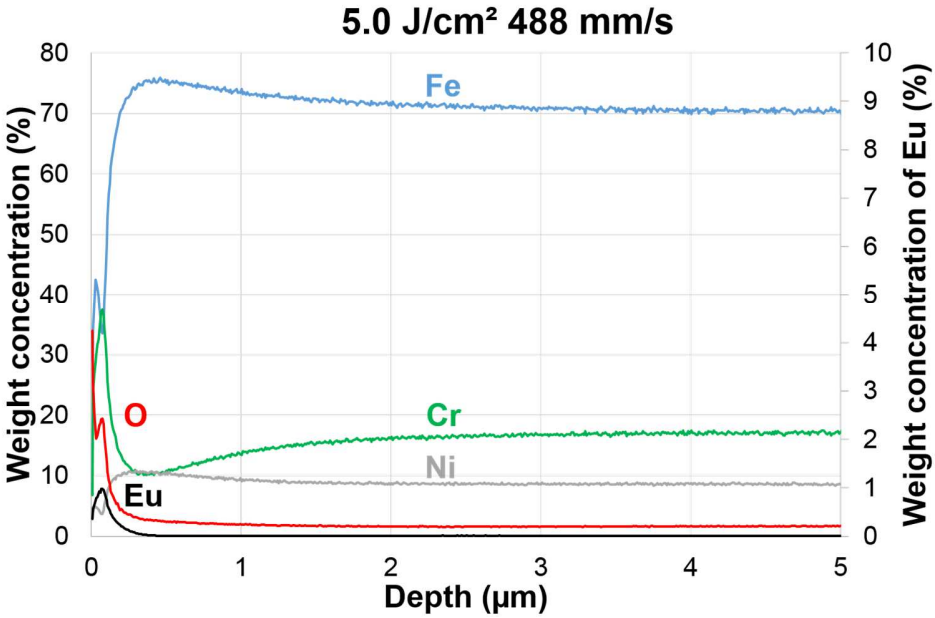

Figure 7. Glow discharge mass spectrometry (GD-MS) profile of oxidized sample after laser treatment 2

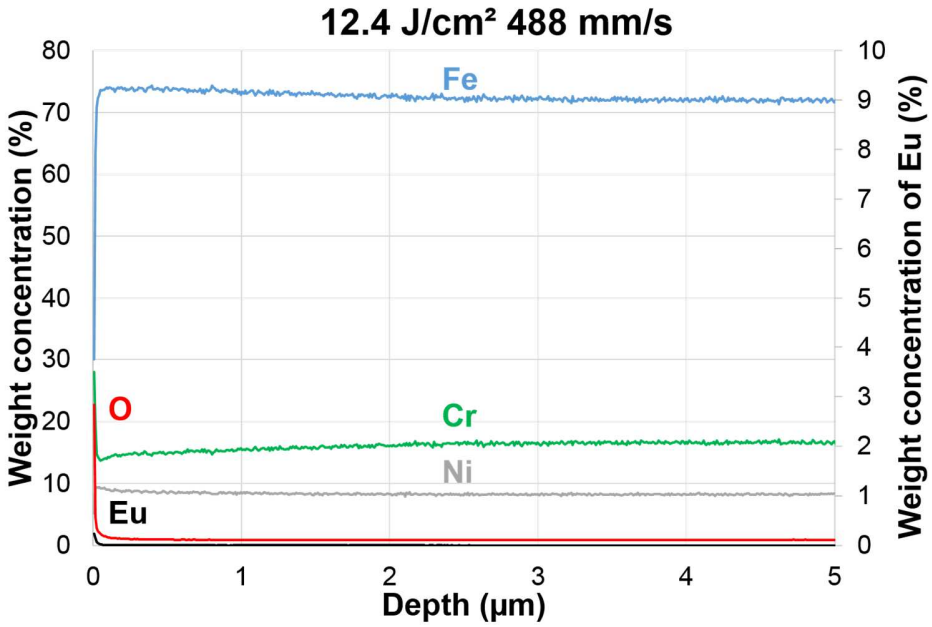

Figure 8. Glow discharge mass spectrometry (GD-MS) profile of oxidized sample after laser treatment 3

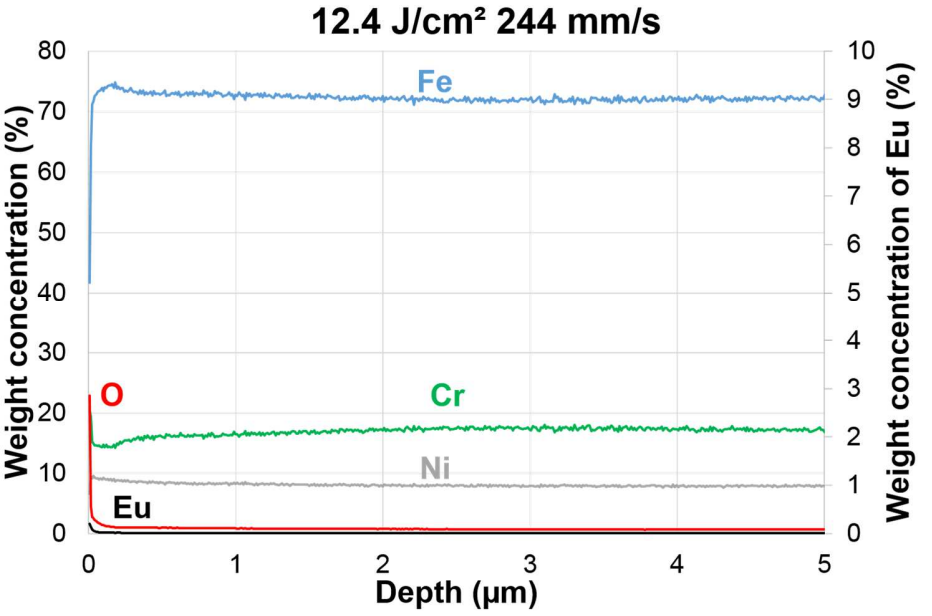

Figure 9. Glow discharge mass spectrometry (GD-MS) profile of oxidized sample after laser treatment 4

From the above results, we note that in order to achieve efficient decontamination, the laser fluence needs to be maximized (in our case, 12.4 J/cm^2) and the scanning speed must be limited to 488 *mm/s* (80% laser spot overlapping). In our study, treatment 3 appeared to correspond to the optimal set of parameters for the cleaning of oxidized and contaminated samples.

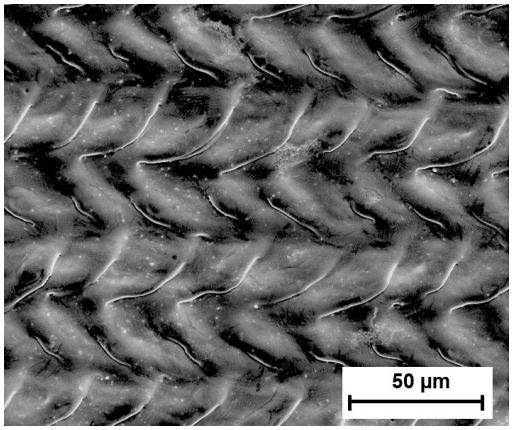

Figure 10. Scanning electron microscopy secondary electron (SEM-SE) (15 kV, 2 nA, M = ×500) image of sample after treatment 3

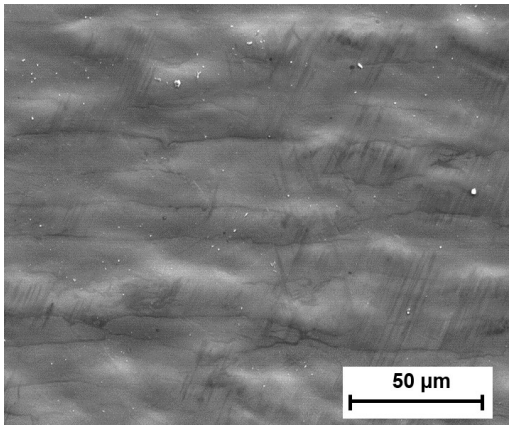

Figure 11. Scanning electron microscopy secondary electron (SEM-SE)(15 kV, *2* nA, M = *×500) image of sample after treatment 4*

3.2. Residual contamination

After laser cleaning, the residual contamination needs to be treated to assess whether complete decontamination has been achieved. In our study, in order to determine the localization of the residual Eu-contamination, we performed the characterization of the Eu distribution at lower concentration range. Following previous studies [6][15][16][35], we prepared samples with Eu contamination and used the GD-MS technique in order to obtain the depth-wise distribution of the contaminant with a detection limit of 100 *ng/g*. The corresponding results are presented in Figure 12. We observe a depth-wise Eu contamination with a weight concentration maximum of 0.025% around a depth of 2.2 *μm* in the oxidized sample before cleaning. This contamination is considered low in comparison to the average Eu contamination of 0.95% in the superficial oxide layer.

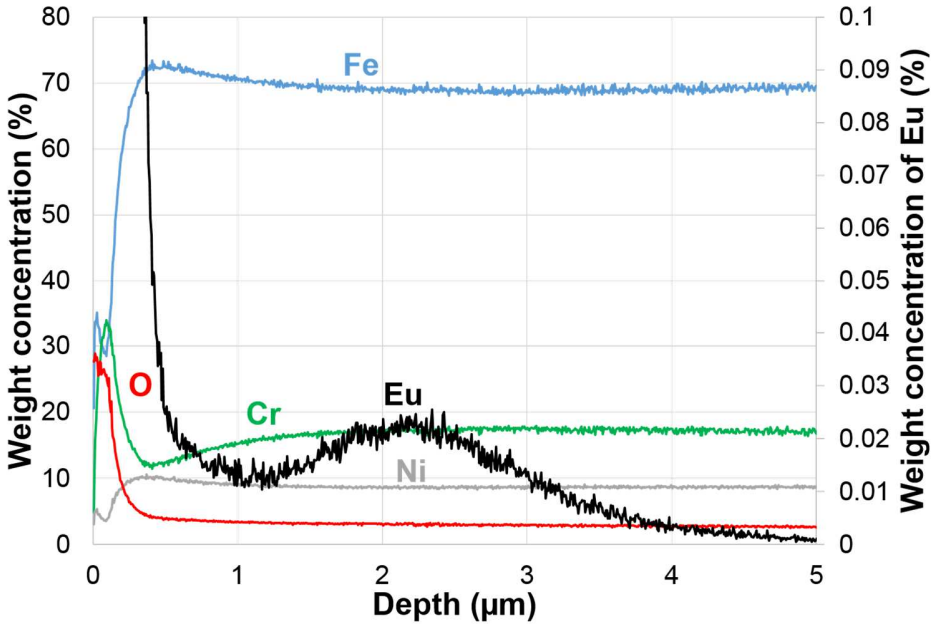

Figure 12. Glow discharge mass spectrometry (GD-MS) profile of contaminated and oxidized sample before cleaning. Relative to the Eu concentration scale in Figure 2, the scale of Eu concentration has been modified to visualize depth-wise contamination.

Eu impregnation deep in the metal bulk occurred during the preparation of the sample by superficial fusion and oxidation due to the laser (see Section 2.3.) [28]. We speculate that impregnation was induced by Eu diffusion into the metallic bulk, and it was enhanced by increase in the surface temperature.

The fact that Eu penetrated to a depth of 2.2 μm affords us information about the dimensions of the melt zone or at least the thermally affected zone during laser oxidation.
Once the residual contamination was identified, its evolution was analyzed for cleaning treatments 2 and 3 (Figure 13). At low fluence (F = 5.0 J/cm^2, treatment 2), the total depth-wise contamination appeared to be reduced but the distribution was not modified, whereas at 12.4 J/cm^2 (treatment 3), the distribution of the contaminant changed, and the resulting weight concentration was <0.005%. These results are consistent with the cleaning efficiency evolution listed in Table 2. For both treatments, the maximum Eu concentration decreases, which indicates that the contamination was ejected by thermal effects during the laser irradiation. The sample is indeed believed to be thermally affected by the laser energy to a depth of a few micrometers, thereby implying Eu diffusion from the bulk to the surface.
The reason why the surface (and near surface) chemistry was modified by the laser treatment is surely related to the very fast heating/cooling stage involved in such a process:
(i) Very fast heating/cooling results in smaller grain size and the high amount of grain boundaries enhances Eu diffusion [36][37].
(ii) Very fast heating/cooling promotes solute enrichment across the liquid/solid front during planar solidification. As the planar liquid/solid front moves from the bulk towards the surface, Eu migrates towards the surface.

Finally, a selective oxidation of Eu during the fast heating/cooling stage (in the liquid or solid states) can also result in Eu enrichment of the surface due to its high affinity with oxygen before being vaporized [38]. Since laser surface melting process involves cooling rates of more than 10^{10} K/s and solidification rates superior to 1 m/s, physical mechanisms are complicated to explain. Constitutional undercooling of course exists but most of all, the solid/liquid interface has no time enough to be deformed, this partially explains why solidification front remains planar. This assumption could mostly be attributed to a solute trapping phenomenon, which is suspected to occur for strongly out of equilibrium conditions. It is mostly characterized by partition coefficients between solid and liquid tending to 1 for very high solidification rates. In that case, diffusion coefficients are not sufficient to allow Eu migration toward the surface [39][40].
Considering all those possible thermo-physical phenomena, the Eu migration is suspected to come from a combination of factors. They involve Eu rejection

across the liquid/solid planar front during solidification, and a Eu migration towards the surface favored by its affinity with oxygen.

In conclusion, the heating regime used during the oxidation may have induced residual contamination; however, our parametric study indicated that with sufficient laser energy density, the contamination can be ejected without penetration in the sample bulk. More experiments at higher laser fluences and the same scanning speed need to be carried out in order to increase the decontamination efficiency.

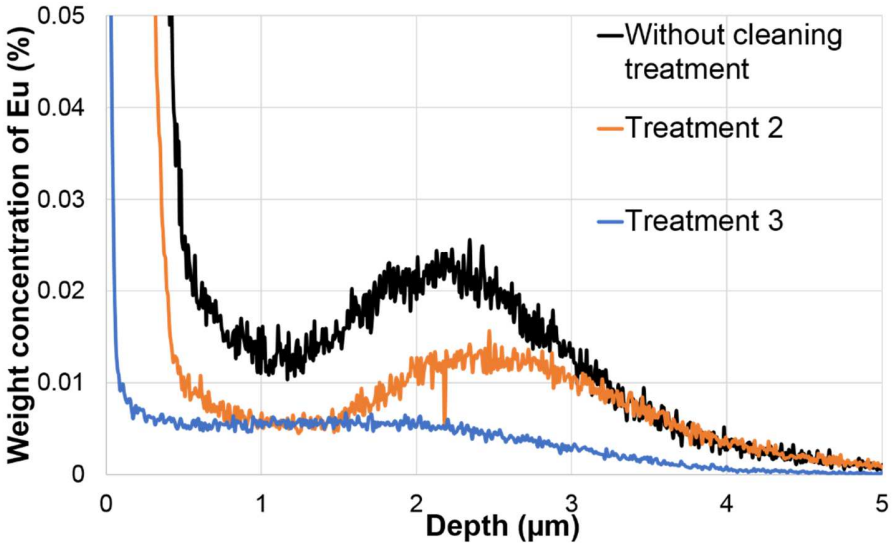

Figure 13. Evolution of Eu concentration for treatments 2 and 3

3.3. Characterization of collected matter

To better understand the ablation mechanisms involved and to choose the appropriate contaminant filter for industrial application, we characterized the removed contamination by means of different techniques. During laser cleaning, the ablated matter was collected by a filter through a plastic tube, and its mass and chemical composition were determined by ICP-OES.

A cascade impactor connected to the ablation chamber was used to measure the particle size distribution. This distribution measurement was performed for treatments 2 and 3 in order to evaluate the influence of the laser beam energy on the ablated matter.

3.3.1. Chemical composition

Particle composition analysis was performed by means of ICP-OES after collection of the entire volume of ablated particles in a cellulose filter (25 mm diameter, 0.45 μm of pore size, Whatmann). The filters were then diluted in acid for analysis. The oxygen present in the ablated matter could not be determined because of the lack of solubilization of this element under our analytical conditions.

Element	Fe	Cr	Ni	Mn	Eu
Treatment 2	59.77	32.47	4.43	2.30	1.03
Treatment 3	69.25	20.29	8.28	1.56	0.62

Table 3. Chemical composition (%) of collected matter after laser decontamination as determined by inductively coupled plasma/optical emission spectrometry (ICP-OES)

The results (Table 3) indicate that the overall composition of the matter collected by the filters in treatment 2 is similar to the oxide composition determined in section 2.4 as Fe_3O_4 and/or $FeCr_2O_4$, whereas for treatment 3, the composition is closer to that of the metallic bulk (see Table 1). The composition of the collected matter was also analyzed to assess the removed mass and estimate the ablated depth. Assuming that the oxide layer had a constant thickness of 0.13 ± 0.03 μm, the ablated thickness was calculated to be 0.11 μm for treatment 2 and 0.37 μm for treatment 3 at a higher fluence of 12.4 J/cm^2. We estimated the ablated thickness by considering the mass due to the ejected oxide, with a density of 5.2 g/cm^3, and also the mass of the ablated metal, with a density of 7.9 g/cm^3. These results are consistent with the observation that for treatment 2, the ablated matter is composed of Eu-contaminated oxide and that the fluence of 5.0 J/cm^2 is not sufficient to ablate the whole oxide thickness. For both treatments, the ablated depth was less than the contaminated depth of 2.2 μm. These results show that residual Eu cleaning is induced by the diffusion of contamination to the surface and not by mechanical ablation of the whole contamination depth of ≈ 2 µm.

3.3.2. Size distribution

Laser cleaning was performed with the application of parameters presented in Table 2 for a small portion of the sample of 3 mm × 3 mm to avoid saturation of the ELPI system. The Figure 14 presents the size distribution of all the collected particles for treatments 2 and 3 and scanning

electron microscopy backscattering electron (SEM-BSE) images of collected particles obtained with treatment 3.

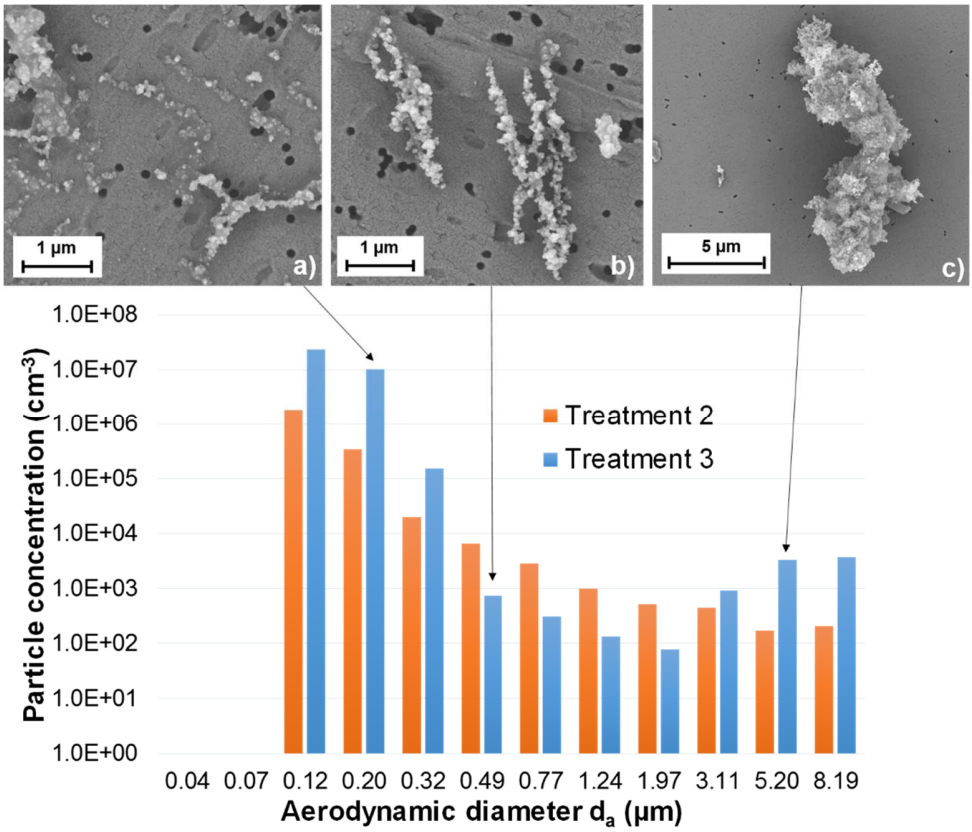

Figure 14. Size distribution of collected particles for treatments 2 and 3 and scanning electron microscopy backscattering electron (SEM-BSE) (10 kV, *0.5* nA*) images of collected particles obtained with treatment 3 at* F = *12.4* J/cm^2*: (a)* d_a = *200* nm *(*M = *×15000); (b)* d_a = *490* nm *(*M = *×15000), and (c)* d_a = *5.20* µm *(*M = *×5000)*

Firstly, it is noteworthy that no individual nanoparticles with dimensions smaller than 100 *nm* were detected by ELPI. For both laser energy densities, the maximal size concentration was found for the filter stages with diameter d_a = 120 *nm* and 200 *nm*. The SEM images of the particles collected by filters with a small diameter size (Figure 14(a) and (b)) indicate the presence of micrometric aggregates of primarily submicrometric particles. The measured diameter d_a is related to the primary particle size and not the actual dimensions of the collected aerosols on the filters [41][42]. According to the literature [43][44], these chainlike structures are characteristic of a

nanosecond pulsed laser regime and appear as the result of several mechanisms such as particle condensation, coalescence, and agglomeration. During nanosecond laser irradiation, the material is first vaporized, and coalescence occurs when the temperature and the pressure drop quickly in the vapor plume [7][43]. During the cooling process, the primary nanoparticles aggregate by collision and form a submicrometric chain, as observed in Figure 14(a) and (b). Moreover, the ablation of the submicrometric oxide layer is speculated to occur by thermomechanical ejection because of the mechanical strains between the oxide layer and the metallic substrate.

For treatment 3 with laser fluence of 12.4 J/cm^2, micrometric aerosols were detected and observed by means of the SEM (Figure 14(c)). However, the structure of the collected aggregates was similar to that of the nanoparticle agglomerates (Figure 14(a)). The formation of these micrometric aerosols appears to be induced by the application of higher laser energy and a consequent enhanced density of particles in the ejected matter plume. The agglomeration of particles occurred most probably within the ablation cell or during transport [41]. In addition to matter ablation by evaporation, the recoil pressure of the vapor plume also induces a liquid-phase explosion and the formation of liquid droplets. However, no sign of ejection of liquid droplets was observed on the filters. This result can be attributed to the low laser energy density and absence of instability in the liquid layer [7][45].

The characterization of the collected matter shows that the ablation phenomenon in the case of nanosecond pulsed treatment is mainly induced by melting and vaporization of the metallic target. The rise in energy density leads to enhancement of the ejection of matter by thermal effects, and therefore to increased material removal.

4. CONCLUSION

Studies on nanosecond laser cleaning were performed on stainless steel AISI 304L samples with a non-radioactive Eu-contaminated oxide layer. Our parametric study carried out on the laser fluence and scanning speed highlighted different cleaning regimes. Below the decontamination threshold fluence, cleaning by heating accumulation was performed without ablation of the oxide layer (treatments 1 and 2). An efficient decontamination of 93% (treatment 3) was achieved by application of the maximal available laser

fluence and a spatial overlap limited to 80%. Finally, for a spatial overlap of 90% between laser spots (treatment 4), the cleaning efficiency reached a saturation threshold caused by modification of the laser energy absorption by the surface. Follow-up of the cleaning evolution was performed by analysis of the in-depth element distribution in the decontaminated samples using the GD-MS technique, with a detection limit of 100 *ng/g* for Eu.

The characterization of the initial and residual Eu contaminations for decontamination assessment facilitated a better understanding of the cleaning performances. The analysis also confirmed that optimal cleaning can be achieved by diffusion of the contamination from the metal bulk to the surface. In our case, treatment 3 afforded a cleaning efficiency of 93% without ablation of the entire contaminated depth. A decontamination efficiency up to 97% was obtained after one scan of the sample surface with an average residual-weight Eu concentration of 0.005%.

The ejected matter was collected on filters and measured by means of an ELPI in order to determine the particle size distribution and forms to choose the appropriate filter for efficient collection of the contaminant. These measurements allowed us to theorize on the ablation mechanisms underlying nanosecond laser irradiation. Micrometric chainlike structures of nanoparticles observed under our experimental conditions can be induced by thermomechanical ejection of the oxide layer and vaporization of the metallic bulk, thereby leading to particle condensation during vapor cooling.

Against the backdrop of this work, future studies need to assess the effect of laser setup characteristics such as the laser wavelength, repetition rate, and pulse duration on the cleaning performance. One of the challenges would be to limit the liquid layer formation and study different ablation mechanisms. Furthermore, treatment of samples with surface defects such as cracks or erosion needs to be performed to improve the cleaning efficiency of damaged equipment. In conclusion, we believe that our findings can contribute to the further development of techniques to decontaminate radioactive-material-imbued metallic surfaces.

ACKNOWLEDGMENTS

We would like to thank our colleagues Evelyne Vors and Céline Quéré for their help with the ELPI measurements, Jérôme Varlet for his advice on sample preparation, and Juliette Lambert and Daniel Farcage for their contributions to our laser cleaning experiments.

REFERENCES

[1] Nuclear Energy Agency. *R & D and Innovation Needs for Decommissioning Nuclear Facilities*. 2014.

[2] Nuclear Energy Agency. Nuclear decommissioning: Decontamination techniques used in decommissioning activities: A report by the NEA task group on decontamination. 2009.

[3] J.P. Nilaya, P. Raote, A. Kumar, D.J. Biswas, Laser-assisted decontamination—A wavelength dependent study, Appl. Surf. Sci. 254 (2008) 7377–7380.

[4] D.H. Lister, The transport of radioactive corrosion products in high-temperature water II. The activation of isothermal steel surfaces, Nucl. Sci. Eng. 59 (1976) 406–426.

[5] P. Delaporte, M. Gastaud, W. Marine, M. Sentis, O. Uteza, P. Thouvenot, J.L. Alcaraz, J.M. Le Samedy, D. Blin, Dry excimer laser cleaning applied to nuclear decontamination, Appl. Surf. Sci. 208 (2003) 298–305.

[6] D.W. Bäuerle, Laser Processing and Chemistry, Springer Science & Business Media, 2013.

[7] D. Grojo, Laser-assisted particle removal mechanisms: application to the microelectronics cleaning, PhD thesis, Université de la Méditerranée - Aix-Marseille II, 2006.

[8] A. Anthofer, W. Lippmann, A. Hurtado, Development and testing of a laser-based decontamination system, Opt. Laser Technol. 48 (2013) 589–598.

[9] F. Brygo, Ch. Dutouquet, F. Le Guern, R. Oltra, A. Semerok, J.M. Weulersse, Laser fluence, repetition rate and pulse duration effects on paint ablation, Appl. Surf. Sci. 252 (2006) 2131–2138.

[10] V.P. Veiko, T.Y. Mutin, V.N. Smirnov, E.A. Shakhno, Laser Decontamination of Radioactive Nuclides Polluted Surfaces, Laser Physics. 21 (2011) 608-613

[11] M. Sentis, Ph. Delaporte, W. Marine, O. Uteza, Surface oxide removal by a XeCl laser for decontamination, Quantum Electron. 30 (2000) 495-500.

[12] C. Seo, D. Ahn, D. Kim, Removal of oxides from copper surface using femtosecond and nanosecond pulsed lasers, Appl. Surf. Sci. 349 (2015) 361–367.

[13] Y.F. Lu, M. Takai, S. Komuro, T. Shiokawa, Y. Aoyagi, Surface cleaning of metals by pulsed-laser irradiation in air, Appl. Phys. A, 59 (1994) 281–288.

[14] A. Pereira, Ph. Delaporte, M. Sentis, A. Cros, W. Marine, A.E. Basillais, A.L. Thomann, C. Boulmer-Leborgne, N. Semmar, P. Andreazza, T. Sauvage, Laser treatment of a steel surface in ambient air, Thin Solid Films, 453-454 (2004) 16–21.

[15] A. Kumar, T. Prakash, M. Prasad, S. Shail, R.B. Bhatt, P.G. Behere, D.J. Biswas, Laser assisted removal of fixed radioactive contamination from metallic substrate, Nucl. Eng. Des. 320 (2017) 183–186.

[16] A.J. Potiens, J.C. Dellamano, R. Vicente, M.P. Raele, N.U. Wetter, E. Landulfo, Laser decontamination of the radioactive lightning rods, Radiat. Phys. Chem. 95 (2014) 188–190.

[17] A. Maffini, A. Uccello, D. Dellasega, V. Russo, S. Perissinotto, M. Passoni, Laser cleaning of diagnostic mirrors from tokamak-like carbon contaminants, J. Nucl. Mater. 463 (2015) 944–947.

[18] A. Leontyev, A. Semerok, D. Farcage, P. Y. Thro, C. Grisolia, A. Widdowson, P. Coad, M. Rubel, Theoretical and experimental studies on molybdenum and stainless steel mirrors cleaning by high repetition rate laser beam, Fusion Eng. Des. 86 (2011) 1728–1731.

[19] B.N. Chichkov, C. Momma, S. Nolte, F. von Alvensleben, A. Tünnermann, Femtosecond, picosecond and nanosecond laser ablation of solids, Appl. Phys. A 63 (1996) 109–115.

[20] A.Semerok, C. Chaléard, V. Detalle, S. Kocon, J.-L. Lacour, P. Mauchien, P. Meynadier, C. Nouvellon, P. Palianov, M. Perdrix, G. Petite, B. Sallé, Laser ablation efficiency of pure metals with femtosecond, picosecond and

nanosecond pulses, SPIE, Proceedings of the Conference on High-Power Laser Ablation, Santa Fe, NM, April 26-30, Vol. 3343 (1998) 1049-1055,

[21] M. Stafe, Theoretical photo-thermo-hydrodynamic approach to the laser ablation of metals, J. Appl. Phys. 112 (2012) 123112.

[22] D. Autrique, G. Clair, D. L'Hermite, V. Alexiades, A. Bogaerts, B. Rethfeld, The role of mass removal mechanisms in the onset of ns-laser induced plasma formation, J. Appl. Phys. 114 (2013) 023301.

[23] M. Wautelet, Laser-assisted reaction of metals with oxygen, Appl. Phys. A Mater. Sci. Proc. 50 (1990) 131–139.

[24] N.M. Bulgakova, A.V. Bulgakov, Pulsed laser ablation of solids: transition from normal vaporization to phase explosion, Appl. Phys. A 73 (2001) 199–208.

[25] A. Widdowson, J.P. Coad, D. Farcage, D. Hole, J. Likonen, T. Renvall, A. Semerok, P.-Y. Thro and JET EFDA contributors, Detritiation of JET Tiles by Laser Cleaning, Fusion Science and Technology, Volume: 54 Issue 1 (2008) 51-54.

[26] H. Roche, C. Grisolia, C Hernandez, C Pocheau, A. Semerok, D. Farcage, X. Courtois, N Vignal, Deposited layer removal by laser ablation: from laboratory to Tore Supra integration, Phys. Scr. T138 (2009) 014028 (4pp)

[27] A.Widdowson, J.P.Coad, G. de Temmerman, D. Farcage, D. Hole, D. Ivanova, A. Leontyev, M. Rubel, A. Semerok, A. Schmidt, P.-Y. Thro and JET-EFDA Contributors, Removal of beryllium-containing films deposited in JET from mirror surfaces by laser cleaning, Journal of Nuclear Materials 415 (2011) S1199–S1202.

[28] L. Carvalho, W. Pacquentin, M. Tabarant, H. Maskrot, A. Semerok, Growth of micrometric oxide layers to explore laser decontamination of metallic surfaces, EPJ Nuclear Sci. Technol. 3 (2017) 30.

[29] Luisa Carvalho. Etude de l'interaction laser surface pour le développement de procédé de décontamination de surfaces métalliques

avec fissures micrométriques par ablation laser. PhD thesis, Université Paris-Saclay, 2018.

[30] R. Muñiz, L. Lobo, T. Kerry, C.A. Sharrad and R. Pereiro. Depth profile analysis of rare earth elements in corroded steels by pulsed glow discharge-time of flight mass spectrometry. Journal of Analytical Atomic Spectrometry, 32(2017) : 1306-1311.

[31] D.P. Adams, V.C. Hodges, D.A. Hirschfeld, M.A. Rodriguez, J.P. McDonald, P.G. Kotula, Nanosecond pulsed laser irradiation of stainless steel 304L: Oxide growth and effects on underlying metal, Surf. Coat. Tech. 222 (2013) 1–8.

[32] B. Sallé, Etude de l'interaction laser-matériau appliquée à l'analyse élémentaire des solides, PhD thesis, Orléans, 1999.

[33] A. Leontyev, Laser decontamination and cleaning of metal surfaces: modelling and experimental studies, PhD thesis, Université Paris Sud Paris XI, 2011.

[34] G. Raciukaitis, M. Brikas, P. Gecys, M. Gedvilas, Accumulation effects in laser ablation of metals with high-repetition-rate lasers, Proc. SPIE 7005 (20085) 70052L.

[35] Y. Kameo, M. Nakashima, T. Hirabayashi, Removal of metal-oxide layers formed on stainless and carbon steel surfaces by excimer laser irradiation in various atmospheres, Nucl. Technol. 137 (2002) 139–146.

[36] F. Weinberg, Grain boundaries in metals, Progress in metal physics, vol 8 (1959) 105-128

[37] C. Cui, J. Hu, Y. Liu, K. Gao, Z. Guo, Formation of nano-crystalline and amorphous phases on the surface of stainless steel by Nd:YAG pulsed laser irradiation, Applied surface Science 254 (2008) 6779-6782

[38] P.R. Wilson, Z. Chen, The effect of manganese and chromium on surface oxidation products formed during batch annealing of low carbon steel strip, Corrosion science 49 (2007) 1305-1320

[39] W.A. Tiller, K.A. Jackson, J.W. Rutter and B. Chalmers, The redistribution of sulute atoms during the solidification of metals, Acta metallurgica, vol 1 (1953) 428-437

[40] W. Kurtz, B. Giovanola and R. Trivedi, Theory of microstructural development during rapid solidification, Acta metallurgica, vol 34 No 5 (1986) 823-830

[41] H.-R. Kuhn, J. Koch, R. Hergenröder, K. Niemax, M. Kalberer, D. Günther, Evaluation of different techniques for particle size distribution measurements on laser-generated aerosols, J. Anal. At. Spectrom. 20 (2005) 894–900.

[42] F.A. Barreda, Etude expérimentale et modélisation des potentialités de la technique LIBS (ablation laser couplée à la spectroscopie) pour l'analyse directe des solides, PhD thesis, Universit'e Claude Bernard-Lyon I, 2010.

[43] M. Ullmann, S.K. Friedlander, A. Schmidt-Ott, Nanoparticle formation by laser ablation, J. Nanoparticle Res. 4 (2002) 499–509.

[44] M. Hola, V. Konecna, P. Mikuska, J. Kaiser, V. Kanicky, Influence of physical properties and chemical composition of sample on formation of aerosol particles generated by nanosecond laser ablation at 213 nm, Spectrochim. Acta Part B At. Spectrosc. 65 (2010) 51–60.

[45] R. Hergenröder, Laser-generated aerosols in laser ablation for inductively coupled plasma spectrometry, Spectrochim. Acta Part B At. Spectrosc. 61 (2006) 284–300.

Decontamination efficiency

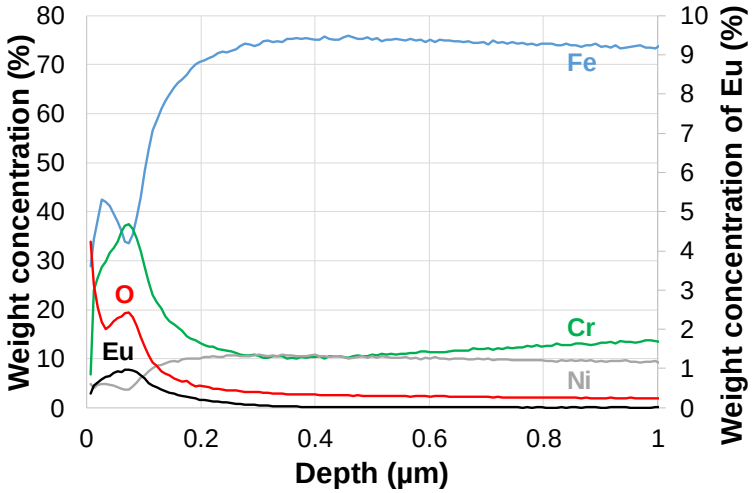

GD-MS in-depth element profile

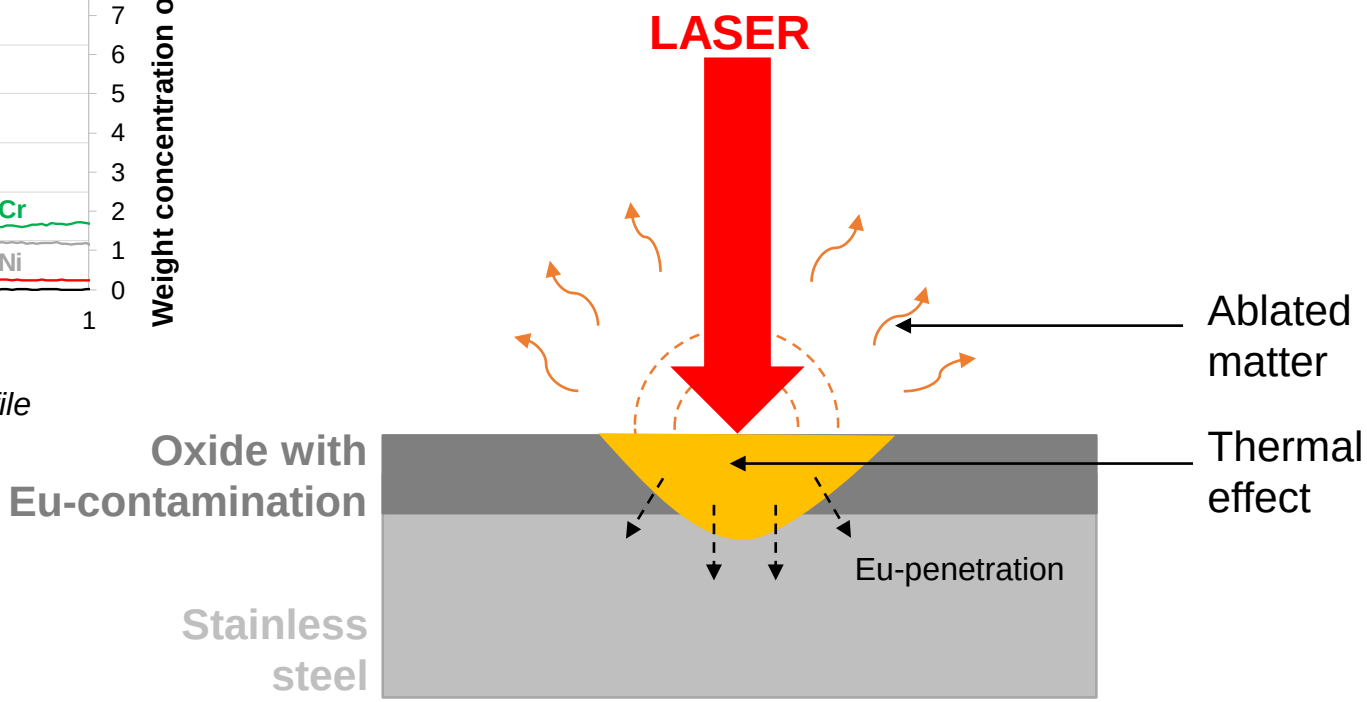

Laser cleaning

Ablated matter characterization

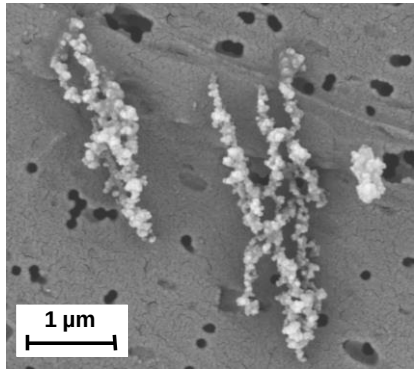

SEM image of ablated matter (M = x15000)